FIB/SEM Tomography Segmentation by Optical Flow Estimation

Riko Moroni[1], Simon Thiele[2, 3] *

1 Laboratory for MEMS Applications, IMTEK Department of Microsystems Engineering, University of Freiburg, 79110 Freiburg, Germany

2 Forschungszentrum Jülich GmbH, Helmholtz-Institute Erlangen-Nürnberg for Renewable Energy (IEK-11), 91058 Erlangen, Germany

3 Department of Chemical and Biological Engineering, Friedrich-Alexander-Universität Erlangen-Nürnberg, 91058 Erlangen, Germany

* Corresponding author

Abstract

Focused ion beam/scanning electron microscopy tomography (FIB/SEM tomography) is the method of choice for the tomographic reconstruction of mesoporous materials systems in various fields such as batteries, fuel cells, filter applications or composite materials. However, due to so called shine-through artifacts in FIB/SEM tomographies of porous materials, their segmentation into pore space and solid material is a nontrivial task. Here, an optical flow-based method that utilizes shine-through artifacts for segmentation is introduced. Subsequently, the performance of the method is discussed by means of tomographic datasets of a polymer electrolyte fuel cell catalyst layer and a lithium ion battery composite electrode. Previous, manual segmentations of these datasets allow the evaluation of the results – for the catalyst layer an accuracy of 86.6 % and a precision of 84.0 % is reached. In both cases, the optical flow-based approach gives significantly better results than comparable segmentations obtained from gray-value threshold binarization.

Keywords: Focused ion beam, scanning electron microscope, tomography, segmentation, porous materials systems, optical flow estimation

1. Introduction

Porous materials systems are found in all applications that have a necessity for large surface areas per volume. In the field of electrochemical energy systems, proton-exchange membrane fuel cells (PEMFCs) and lithium-ion batteries (LIBs) are prominent examples for this: While in PEMFCs oxidation and reduction reaction are usually facilitated by a surface bound catalyst [1], the incorporation of lithium ions into the active material of LIB composite electrodes depends on a sufficiently high active material surface area [2]. Consequently, catalyst layers of PEMFCs and composite electrodes of LIBs are usually highly porous. However, the surface area in these electrochemical cells can only be utilized if the transport of fuel or lithium ions, respectively, through the porous layers of the cell can be facilitated in an effective way. A common measure for this is the tortuosity: If one considers paths through the pores of a porous layer, the tortuosity is the ratio between the path lengths to the thickness of the layer [3]. This leads to a dilemma: while porous layers with large surface area per volume exhibit high tortuosity, porous layers with low tortuosity have comparably small surface area. The interplay between these two properties as well as their evolution over the lifetime of the electrochemical cells thus makes the understanding and optimization of the morphology of the porous cell components an important field of research [4,5].

An important tool to investigate the morphological properties of porous layers is their partial tomographic reconstruction and subsequent computational analysis [6]. For mesoporous materials systems with pore and grain sizes in the range of 2–50 nm, such as PEMFC catalyst layers and LIB composite electrodes, focused ion beam/scanning electron microscopy tomography (FIB/SEM tomography) is an appropriate tomographic technique [7]. In this technique, a region of interest (ROI) in the sample is split into a series of thin sections. Each of these sections is imaged by SEM and subsequently ablated with the FIB, enabling the imaging of the next section (Figure 1). Depending on the desired resolution and size, a tomographic dataset usually consists of several hundred images. This 2D image series can be turned into a 3D image by a number of geometrical operations. Resolutions of up to 3 nm in-plane and 9 nm through-plane with respect to the SEM image plane are feasible [7]. After acquisition, the tomographic dataset has to be segmented in order to perform further analysis.

Segmentation is the step of labelling each pixel of the image stack, for example as ‘pore’ or ‘solid’. As this step is obviously crucial for the quality of the subsequent analysis, it has to be performed with care. Unfortunately, in the case of FIB/SEM tomography of highly porous materials, common segmentation techniques that solely rely on the contrast between materials are bound to fail [8]. The reason for this are so called shine-though artifacts: Since the pores in the sample are transparent for the electron beam of the SEM, each image also shows solid material that should be attributed to subsequent images. An example of the resulting shine-through artifacts is depicted in Figure 1c. The segmentation of the actual solid material for each slice is thus very demanding. One approach to solve this segmentation problem is to simply avoid it by filling the pore space in the sample prior to tomography, either by infiltration of metal [9], resin [10,11], or by means of atomic layer deposition [12]. However, each of these approaches has its drawbacks. While infiltration exerts a non-negligible force on the sample and might alter it, atomic layer deposition is not always available and has limited penetration depth. Furthermore, it might not always be easy to find a filler material that has proper contrast in the SEM to all the materials in the sample. If filling of the pore space is not feasible, segmentation has either to be done manually, which is an extremely tedious process for several hundred images, or tailor-made segmentation algorithms that rely on the detection of shine-though artifacts in the tomographic data have to be used [13,14]. However, depending on the sample under consideration, these algorithms do not always lead to satisfactory results [15].

To this end, a new segmentation approach that is based on existing algorithms for optical flow estimation is introduced here. This segmentation approach is then evaluated by means of two previously published datasets that have been segmented either completely or partially by hand. The results of the evaluation are followed by a discussion and finally some concluding remarks. Furthermore, a MATLAB [16] implementation of the algorithm as well as an example application are provided to the reader in the supplementary material.

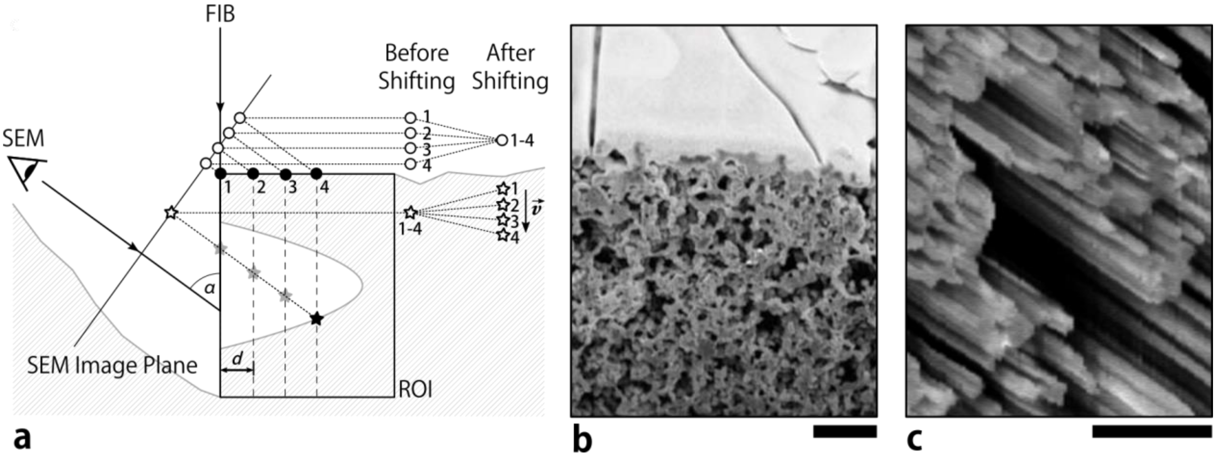

Figure 1: FIB/SEM tomography acquisition process. (a) Schematics of the acquisition geometry. Since the FIB milling plane is tilted w.r.t. the SEM beam direction (angle α), the features marked by filled circles are mapped to different points in the SEM imaging plane. In order to compensate for this, subsequent images of the tomography are shifted w.r.t. each other. This leads to an apparent movement of features that lie behind the FIB milling plane (star symbol), the so called shine-through artifacts. See section 2.1 for more details. (b) A typical image of a FIB/SEM tomography dataset. In the upper area of the image fiducial lines are visible. These lines can be used for the registration of subsequent images and to check the FIB milling distance. (c) A side-view of a FIB/SEM tomography dataset after registration. Shine-through artifacts are clearly visible as diagonal lines. These artifacts are a major obstacle for dataset segmentation.

2. Materials and Methods

Since the appearance of the shine-through artifacts in the dataset obtained by FIB/SEM tomography depends on the setup, the geometric transforms that are necessary to obtain the 3D grayscale image from the 2D SEM image series are recapitulated in this section. Subsequently, the optical-flow-based segmentation approach is described. Finally, the datasets and that are employed for the evaluation of the algorithm as well as the respective segmentation approaches are presented in detail.

2.1. FIB/SEM Tomography Data Processing

A side-view schematic of a general FIB/SEM tomography setup is given in Figure 1a. During tomography, the sections labeled 1–4 are imaged with the SEM and subsequently milled away with the FIB. This results in a sequence of SEM images similar to the one depicted in Figure 1b. In a first step, consecutive images in this sequence have to be properly registered or aligned with each other in order to account for thermal drift of the sample. As the quality of alignment influences the optical flow between images, this step has to be performed with caution. Subsequently, two major transformations have to be applied to each image of the sequence in order to compensate for the acquisition angle α between electron and ion beam. First, each image has to be shifted downwards by $d \cdot \cos\alpha$, where d is the thickness of each sample slice, with respect to its preceding image. This ensures that features, which are physically at the same level, such as the circle symbols at the top of the ROI in the Figure 1a, also appear at the same level in the final tomographic reconstruction. Second, each image has to be stretched by a factor of $1/\sin\alpha$ in order to compensate for the angle between the electron and the ion beam.

After these transformations, features which are visible in several consecutive images ‘move’ along the vertical axis along the image sequence. This is illustrated in Figure 1a by means of the star symbol. These ‘movements’ result in shine-though artifacts, which are visible as diagonal lines perpendicular to electron and ion beam in the final transformed dataset (Figure 1c). In consequence does the detection of vertical motion correspond to the detection of features in the background. The problem of solid material segmentation can thus be interpreted as a problem of motion detection in the 3D FIB/SEM image sequence.

2.2. Optical-Flow-Based FIB/SEM Tomography Segmentation

Optical flow estimation describes the process of estimating the displacement field between two subsequent images in of an image sequence. The displacement field denotes magnitude and direction of motion for each pixel in the image pair. In this paper, classical variational models for optical flow estimation are considered [17,18], which aim at the minimization of an energy functional given by

$$\begin{aligned} E(\boldsymbol{u},\boldsymbol{v}) = \sum_{i,j} & \rho\left(I_1(i,j) - I_2\big(i+u_{i,j}, j+v_{i,j}\big)\right) \\ & + \lambda\left(\rho\big(u_{i,j}-u_{i+1,j}\big) + \rho\big(u_{i,j}-u_{i,j+1}\big) + \rho\big(v_{i,j}-v_{i+1,j}\big) + \rho\big(v_{i,j}-v_{i,j+1}\big)\right). \end{aligned} \tag{1}$$

Here, $\boldsymbol{u}$ and $\boldsymbol{v}$ denote the displacement fields in vertical and horizontal direction, respectively. i and j represent row and column indices of the images, where I_1 and I_2 mean the color value of the respective image at the specified row and column. $\rho(x) = (x^2 + \epsilon^2)^a$ is a generalized Charbonnier penalty function and λ an adjustable parameter. Simply put, the first addend in the sum compares the similarity in intensity between two images, while the second addend penalizes strong deviations between the displacement values of neighboring pixels. The ratio between the influence of these two contributions is set by λ.

If the concept of optical flow estimation is applied to the apparent movement of shine-through artifacts as described in section 2.1, equation (1) can be drastically simplified: Only movement in the vertical direction of the images by a fixed amount $l = d \cdot \cos\alpha$ has to be considered. This correspond to $v_{i,j} = 0$ and $u_{i,j} = l \cdot x_{i,j}$, with $x_{i,j} \in \{0,1\}$. Here, $x_{i,j} = 1$ corresponds to moving pixels (that is, background), and $x_{i,j} = 0$ to stationary or solid pixels.

Putting this into equation (1), the energy functional reads

$$E(\boldsymbol{x}) = \sum_{i,j} \rho\left(I_1(i,j) - I_2\big(i + l\cdot x_{i,j}, j\big)\right) + \lambda\left(\rho\left(l\big(x_{i,j}-x_{i+1,j}\big)\right) + \rho\left(l\big(x_{i,j}-x_{i,j+1}\big)\right)\right), \tag{2}$$

Since $x_{i,j}$ is either zero or unity and l is fixed, the functional can be further simplified to

$$E(\boldsymbol{x}) = \sum_k \Delta I_k x_k^2 + \lambda'(x_k^2 + x_{k+1}^2 - 2x_k x_{k+1} + x_k^2 + x_{k+m}^2 - 2x_k x_{k+m}) = \boldsymbol{x}^T Q \boldsymbol{x}. \tag{3}$$

In equation (3), row and column indices have been replaced by linear indexing with $k = i + m \cdot (j-1) \in \{1, \ldots, . n\}$, where m is the number of rows in the images and n denotes the total number of pixels per image. This allows the introduction of matrix notation and of the symmetric $n \times n$ matrix Q with entries $q_{r,s} = \delta_{r,s}(\Delta I_r + 4\lambda') - \lambda'\big(\delta_{r,s+1} + \delta_{r,s-1} + \delta_{r,s+m} + \delta_{r,s-m}\big)$.

Furthermore, the abbreviations $\lambda' = \lambda \cdot \big(\rho(l) - \rho(0)\big)$ and $\Delta I_k = \rho\big(I_1(k) - I_2(k+l)\big) - \rho\big(I_1(k) - I_2(k)\big)$ have been used. If not only two, but multiple consecutive images should be compared, ΔI_k can be formulated as

$$\begin{aligned} \Delta I_k = {} & \rho(\|(I_1(k) - I_2(k+l), I_1(k) - I_3(k+2l), \ldots)^T\|_2) \\ & - \rho(\|(I_1(k) - I_2(k), I_t(k) - I_3(k), \ldots)^T\|_2), \end{aligned} \tag{4}$$

where $\|\cdot\|_2$ denotes the L^2 norm. In addition, the energy functional can be altered in order to not only consider the displacement field between two subsequent images, but of the whole image stack. The functional then reads $E(\boldsymbol{x}') = \boldsymbol{x}'^T Q' \boldsymbol{x}'$, with $\boldsymbol{x}' = (x_1, \dots, x_N)^T$, where N is number of pixels in the 3D image stack, and $q'_{r,s} = \delta_{r,s}(\Delta I_r + 6\lambda') - \lambda'(\delta_{r,s+1} + \delta_{r,s-1} + \delta_{r,s+m} + \delta_{r,s-m} + \delta_{r,s+n} + \delta_{r,s-n})$.

The minimization of the energy functional given by equation (3) w. r. t. $x_k \in \{0, 1\}$ yields the optical flow of the FIB/SEM tomography reconstruction. This optical flow corresponds to the segmentation of the reconstruction into solid (stationary pixels) and pore (moving pixels). Thus, the problem of FIB/SEM tomography segmentation can be formulated as a quadratic binary optimization problem in the form of equation (3). Unfortunately, these problems are known to be NP-hard and therefore cannot be solved in polynomial time, making its exact solution not feasible for segmentation applications [19].

In this publication, a simulated-annealing-based heuristic implementation is used in order to find a solution that is close to the global minimum of the functional [20]. In this approach, a random solution $\boldsymbol{x}$ and a defined temperature $T > 0$ are initialized. After initialization, elements of the solution vector are iterated in random order. For each element x_k, the change in the value of the energy functional ΔE that corresponds to setting $x_k \leftarrow 1 - x_k$ is computed. If $\Delta E \leq 0$, then the element remains flipped. Otherwise, it gets flipped back with a probability of $1 - \exp(-\Delta E / T)$. After each element of the solution vector has been visited, T is reduced by a predefined factor ('cooling'), and the whole process is repeated. After the desired number of repetitions has been reached, T is raised again ('annealing') to increasingly lower fractions of its initial value. This process of repeated iterating/cooling with subsequent reannealing is re-run a defined number of times.

The idea behind this method is to 'cool' the initial solution vector into a configuration that is close to the global minimum. While in the first run many locally non-optimal x_k are kept, the 'cooling' increases the probability that such local non-optimal x_k are rejected. The purpose of reannealing is to enable convergence to neighboring minima of the objective function. More details on the simulated annealing method with other application examples can be found e.g. in [21].

For this work, the simulated annealing approach has been chosen since a MATLAB implementation of this heuristic gives satisfactory optimization results in the range of a few minutes on a desktop computer, although the number of pixels in 3D images and thus the complexity of the optimization problem is usually very large. Inputs to this implementation are the preprocessed FIB/SEM tomography image stack, the number of images to compare, the acquisition angle α, the cutting distance d, the value of λ', and a threshold value that is used to establish an initial guess to the segmentation solution. The parameters of the generalized Charbonnier penalty function have been fixed at $a = 0.45$ and $\epsilon = 10^{-6}$. The program returns the binary displacement field x in the shape of the input image stack, which equals a solid/pore segmentation. The program code is provided in the supplementary material.

2.3. Exemplary Datasets and Segmentations

In order to assess the quality of the solid/pore segmentation approach described in the preceding section, this method is applied to two previously published FIB/SEM tomographies. The first of the two datasets is a FIB/SEM tomography of a PEMFC cathode catalyst layer (CCL) that was part of a membrane electrode assembly (PRIMEA A510.1 M710.18 C510.4) [22]. The sample consisted of a mixture of platinum-decorated carbon particles and ionomer. This dataset has been manually segmented into pore and solid material, where the segmented part of the tomography has a size of 480 x 480 x 120 pixels and porosity around 59 %. The size of each pixel is given by 3.4 nm x 3.4 nm x 13.6 nm. The second dataset stems from the FIB/SEM tomography reconstruction of a LIB composite electrode [23]. The sample constituted of a composition of $LiMn_2O_4$ active material with a carbon/binder mixture, its porosity was calculated from film thickness to be around 53 %. In this publication, a volume of 550 x 920 x 550 pixels with a pixel size of 33.6 nm x 33.6 nm x 33.6 nm is used. Although this dataset also has been partially segmented into its material domains, the original purpose of this segmentation was the comparison with a much coarser resolved X-ray tomographic reconstruction of the same sample, i.e. the original segmentation does by far not reach the resolution of the tomographic dataset. More details on the acquisition of both tomographic datasets can be found in the original publications, respectively. The CCL dataset is provided to the reader together with the program code in the supplementary material in order to serve as an example.

Since the test datasets exhibit very different morphological characteristics, the optical-flow based segmentation approaches differ in order to accommodate for this.

2.3.1 Dataset I: Fuel-Cell Catalyst Layer

The morphological structure of the fuel cell catalyst layer reconstruction is homogenous throughout the FIB/SEM image sequence: the knotty network of carbon particles and ionomer shows a monomodal grain size distribution with a few slightly bigger agglomerates (Figure 2, Figure 4). The pore network is dominated by a few very large pores with diameters of up to 400 nm, a quarter of the reconstructed volume. Individual materials are hardly distinguishable. Furthermore, some parts of the porous network in the background of the images are affected by the milling process (most probably due to stress relief) and move slightly between subsequent images.

This leads to two major obstacles for the algorithm described in section 2.2: (i) The spherical agglomerates of carbon/ionomer with smooth transitions between brighter and darker regions lack contrast-rich, sharp features. These are however necessary for the unambiguous determination of optical flow. (ii) Some agglomerates are affected in an unexpected way by the milling process, thus hindering the segmentation. This holds especially for large pores, where this effect is visible throughout several images of the sequence. However, both obstacles can be overcome by the simple application of a slight Gaussian blur to each image, followed by resizing all images of the sequence to half their original size. This results in a dataset that is only as large as ¼ of its original. On this scale, however, each pixel contains information of four of the original pixels as well as their neighbors. This makes the determination of optical flow much more robust and, due to the reduced complexity, faster. Furthermore, the problem with feature-free regions is mitigated: With downsizing, the relative amount of boundary pixels between solid and pore increases. Since the interface is usually classified correctly, the loss in resolution is accompanied by a relative increase in properly segmented pixels. In principle, the combination of slight blur and downsizing could be repeated, i.e. one could blur and resize the already resized images again. In this case, the process is well known as Gaussian pyramid [24], and the segmentation results from each stage could be used as an initial guess for the next, more detailed image stack. However, in the present case only one blurring/resizing step was performed.

The overall segmentation process is depicted exemplarily in Figure 2. First, an initial guess of the 'pore' domain is selected by application of a gray value threshold (Figure 2a). Pixels that are initially selected as 'pore' are excluded from segmentation by the algorithm and essentially set the initial boundary conditions for the optimization. In a second step, the initial guess is then refined by the segmentation algorithm described earlier with $\lambda' = 25$ (Figure 2b). Although this intermediate result is already useable, we refine its boundaries on the original, not downsized, dataset. For this, the preliminary segmentation of the solid material is dilated and used to mask the original image data. Subsequently, the pixels of this masked image sequence are brightened with respect to their distance to the solid/pore interface. The result of this process is depicted in Figure 2c. Subsequently, a gray-value threshold binarization is performed and filtered with a 3 x 3 x 3-pixel median filter. This process results in a segmentation that more closely follows the grain of the carbon/ionomer agglomerates than the solely optical-flow-based segmentation. Finally, only the biggest connected element is used as segmentation, thus removing 'floating' pixels.

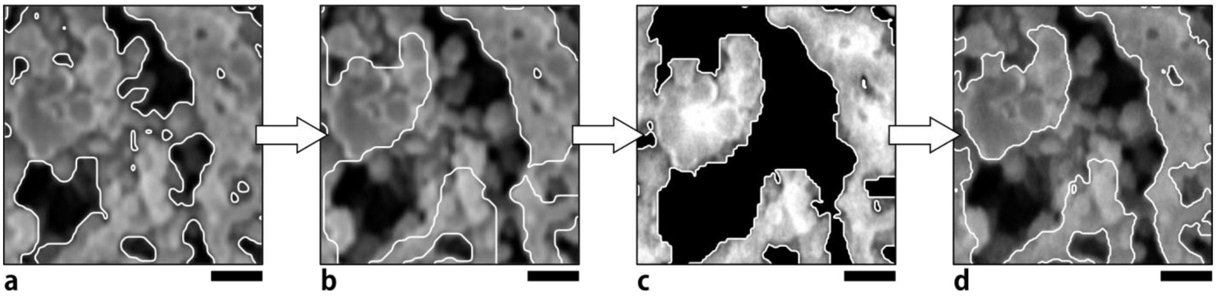

Figure 2: Segmentation of the fuel cell catalyst layer dataset. (a) Initial segmentation of a blurred and downsized version of the original dataset into pore and solid material. This is used as input for the optical-flow-based segmentation (b). (c) The result is used in order to mask and filter the original dataset. (d) The final segmentation that results from a gray value threshold segmentation of c. More details to the segmentation process are given in section 2.3.1. Each scale bar represents 100 nm.

Dataset II: Lithium-Ion Battery Composite Electrode

The morphology of this sample consists of three distinct domains: (i) active material grains with bright contrast, (ii) a fuzzy, fibrous carbon/polymer binder domain, and (iii) the pore space (Figure 3). While the grains are several microns in diameter, the size of the fibers and grains of the carbon/binder domain is in the range of a few tens to hundreds of nanometers and thus close to the image resolution. Due to the sizes of the solid material, the pores exhibit a bimodal pore size distribution: within the carbon/binder domain pore diameters also are around 50—300 nm, however, between active material grains a few very large pores with diameters up to 5 µm are visible. This dataset exhibits some curtaining, i.e. traces of irregular FIB milling, which, just as the stress relief in the previously described sample, hinder the optical flow segmentation. Furthermore, the focus of the SEM is reset within the image sequence, making continuous feature tracking between the affected images difficult. However, by blurring and resizing the image sequence just as described in section 2.3.1, the optical flow segmentation is stabilized and accelerated. In order to accommodate the bimodal pore size distribution, two optical-flow segmentations with differing initial segmentations and λ' values (3 and 15) are generated and combined (Figure 3c). In contrast to the previous subsection, the only post-processing step that is applied is a removal of floating, disconnected pixels after rescaling to the original size of the dataset.

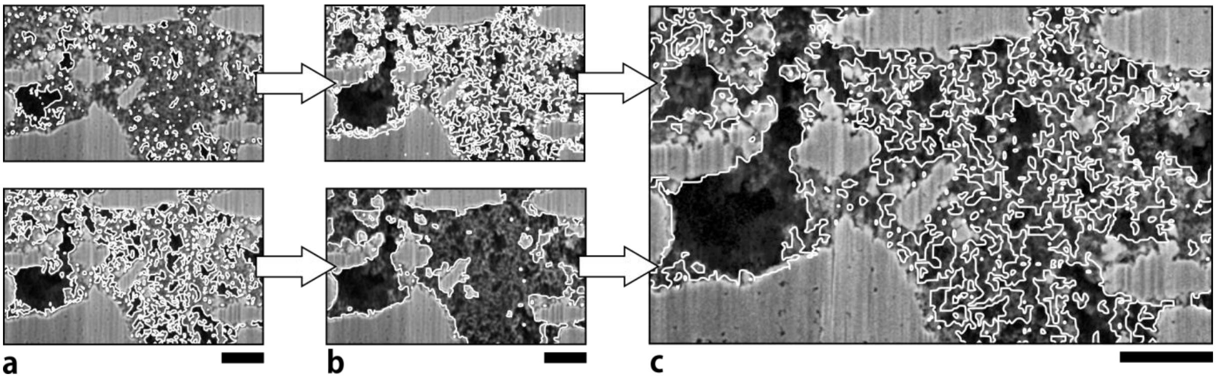

Figure 3: Segmentation of the LIB composite cathode. (a) Initial guesses that are used as input for the optical flow segmentation. Top: Carbon/binder domain. Bottom: Active material. (b) The results of the optical flow segmentation. The combinations of different λ parameters and initial guesses lead to very different results. Top: Carbon/binder domain, λ = 3. Bottom: Active material, λ = 15. For the meaning of the λ parameter, see section 2.2. (c) The final solid material segmentation as a combination of both carbon/binder and active material segmentation. The segmentation of the bigger pores, e.g. in the left of the image, is performed correctly. Each scale bar represents 2.5 µm. More details on the segmentation are given in section 0.

3. Results & Discussion

In order to perform a meaningful evaluation of the segmentation method introduced in this work, its results are not only compared to the original segmentations in this section, but also to simple gray-value threshold segmentations. This simple and common approach thus serves as a benchmark for the reader.

3.1. Dataset I: Fuel-Cell Catalyst layer

Figure 4 presents a visual comparison of the optical-flow-based result to the manually generated reference. From each boundary of the volume, five pixels have been removed in order to exclude minor edge effects that occur in the optical flow process due to a lack of information in these regions. The threshold segmentation in the last row of the figure has been generated by threshold binarization, subsequent 3 x 3 x 3 median filtering and finally removal of disconnected regions. The threshold value has been chosen in a way that the porosity of this segmentation matches the porosity of the reference.

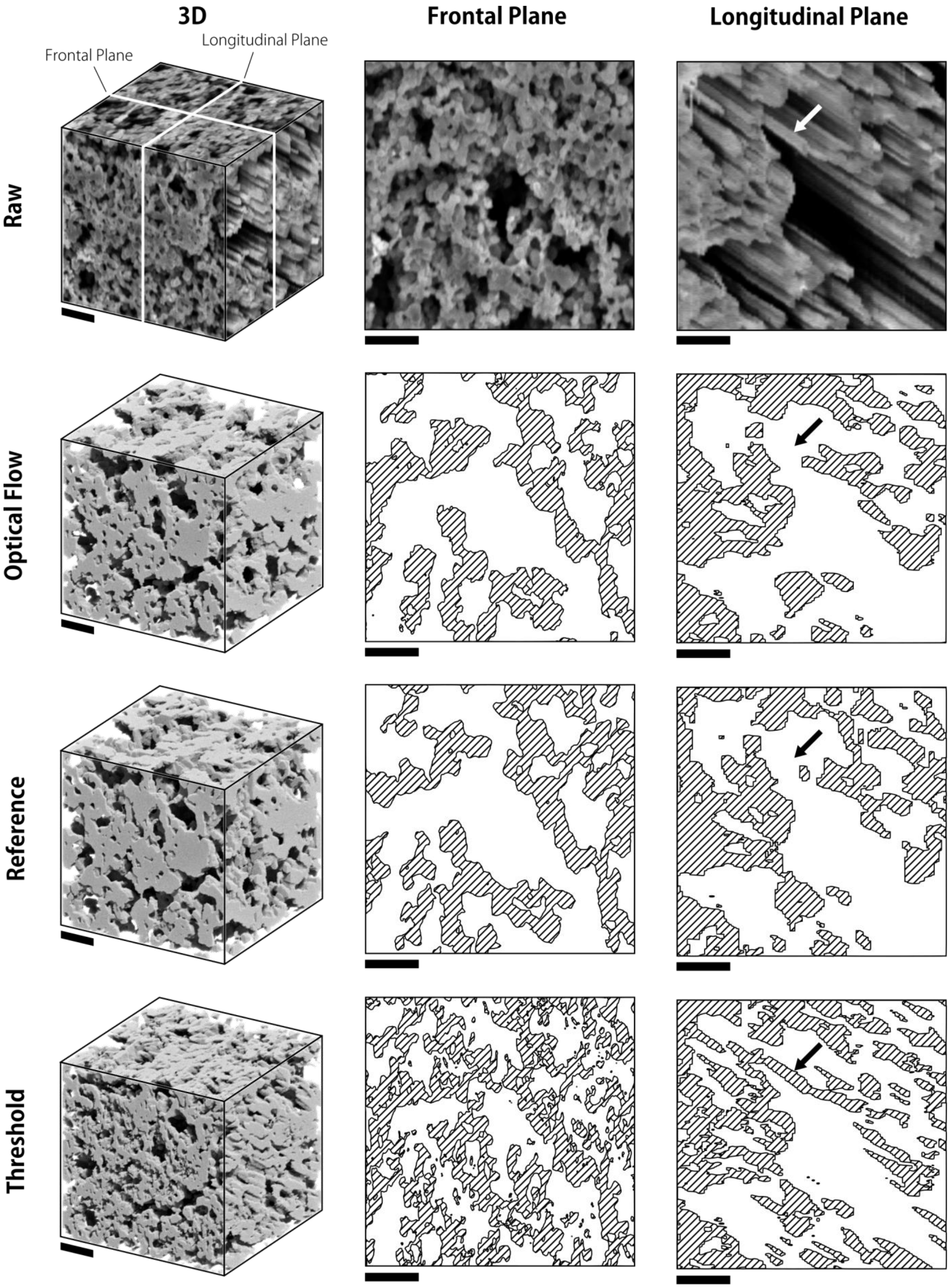

Figure 4: A visual representation of the fuel cell catalyst layer segmentation result. The columns show a 3D representation (left) and the central frontal and longitudinal planes (center and right, respectively). The position of the planes is illustrated in the 3D depiction of the raw data (top left). Each row contains the data denoted to the right. In the center and right columns, solid material is depicted hatched. Each scale bar represents 300 nm.

Table 1: Contingency tables of the fuel cell catalyst layer segmentations. The percentages are given w.r.t. the whole dataset, e.g. 34.5 % of the pixels in the dataset are marked 'solid' in both reference and optical flow segmentation, while 11.4 % are marked 'pore' in the reference, but have been segmented as solid in the threshold segmentation.

		Optical flow		**Threshold**		***Σ***
		solid	pore	solid	pore	
Reference	solid	34.5 %	6.8 %	29.8 %	11.5 %	41.3 %
	pore	6.6 %	52.1 %	11.4 %	47.3 %	58.7 %
Σ		41.1 %	58.9 %	41.2 %	58.8 %	100 %

The figure shows an unambiguous better visual agreement between the optical-flow-based result and the reference when compared to the threshold segmentation. This is evident in both the frontal as well as in the longitudinal plane. In the frontal plane (dashed line, center column in Figure 4), the threshold segmentation gives a much more 'ragged' impression compared to the reference. This effect stems from darker regions in the solid agglomerates (see e.g. the carbon/ionomer agglomerate in the upper left corner in Figure 2d), which are wrongly attributed to the pore space by a simple threshold binarization. However, if the threshold gray value would be changed to compensate for this, the estimated porosity would be severely diminished. A further, more expectable error is visible in the longitudinal plane (dash-dotted line, right column in Figure 4) and exemplarily marked with an arrow: the erroneous segmentation of solid material due to shine-through artifacts. The typical diagonal elongated shapes dominate the visual impression of the threshold segmentation. In contrast, these errors are effectively suppressed in the optical-flow-based segmentation. The general shape of the segmentation matches the reference very well, which is especially clearly visible in the 3D representations in the left column of Figure 4. The quality of the optical-flow result is also representable in numbers (Table 1): Compared to the threshold segmentation, the optical-flow-based approach nearly halves the number of pixels that are wrongly assigned, both for solid and pore pixels. Accuracy (ratio of accurately classified pixels to all pixels) and precision (ratio of correctly assigned solid pixels to all solid pixels) of the optical flow segmentation are significantly better than the threshold segmentation: With 86.6 % and 84.0 %, respectively, both values are circa ten percentage points higher compared to the threshold segmentation (accuracy: 77.1 %, precision 72.3 %). In order to place these values, it might help to recall that a completely random segmentation with 50 % porosity would reach an accuracy of 50 % and a precision of 41.3 %. Finally, it should be noted that manual segmentation is also always subject to error, which easily ranges from 5 % to 10 % w.r.t. the total number of pixels. Therefore, the precision of the optical flow segmentation is difficult to fully assess.

However, although the optical flow procedure substantially improves the segmentation result compared to the threshold segmentation, it obviously does not give perfect results. Main errors are given by a tendency to connect solid agglomerates which are not connected in reality. Furthermore, small pores tend to be ignored. Examples for both effects can be seen in Figure 2d. Nevertheless, the visual agreement to the reference is prominent.

3.2. Dataset II: Lithium-Ion battery composite electrode

In contrast to the fuel cell catalyst layer, the original segmentation of the LIB composite cathode tomography has two major drawbacks: it is both coarse and incomplete. These shortcomings make a quantitative evaluation of the optical flow segmentation unfeasible. However, due to the morphological characteristics of the dataset it is nevertheless worthwhile to again visually compare optical flow segmentation, original segmentation, and threshold segmentation with each other. However, a meaningful ternary segmentation into carbon/binder domain, active material, and pore space, as it is in the reference segmentation, is not feasible by simple threshold application. Therefore, only a segmentation into solid and pore was performed. The relevant threshold value was chosen by visual judgement. As before, the binarization was followed by 3 x 3 x 3 median filtering and removal of disconnected regions. In contrast to the threshold segmentation, optical flow segmentation as described in section 0 allows to distinguish between the three material domains by marking solid material that has not been identified as active material as carbon/binder mixture.

The three segmentations as well as the corresponding raw data are presented in Figure 5. The threshold binarization fails to deliver a proper segmentation of the dataset and results in erroneous solid material segmentation due to shine-though artifacts. This is especially evident in the longitudinal plane (diagonal shapes in the right column of Figure 5), as well as in the region marked with an arrow in the frontal plane (Figure 5, central column). Here, an especially large pore allows the shine-through of an active material grain from the background, leading to a large error in the threshold segmentation. In contrast, the optical-flow-based segmentation approach successfully avoids this error and gives an overall satisfactory to good result, as can be seen in 3D visualization in Figure 5. Especially the agreement between active material segmentations is very high: Optical flow segmentation results in an accuracy of 91.4 % and a precision of 85.6 % in the comparable regions. The most prominent difference between optical flow segmentation and the reference segmentation is the carbon/binder domain. While the reference only roughly marks regions where mesoporous carbon/binder mixture is present, the optical flow segmentation is much more detailed. However, since the resolution of the tomographic dataset is not high enough to fully resolve all features of the carbon/binder mixture, this segmentation is not exact. Figure 5 also shows the vulnerability of the optical flow method for inconsistencies in the FIB milling: The lower left corner of the central raw image (frontal plane) shows slight curtaining, which immediately leads to an erroneous segmentation in this region. Nevertheless, considering that the optical flow result shown in Figure 5 was achieved with only minor post-processing, it can be at least considered an excellent starting point for further improvement with more advanced image processing techniques.

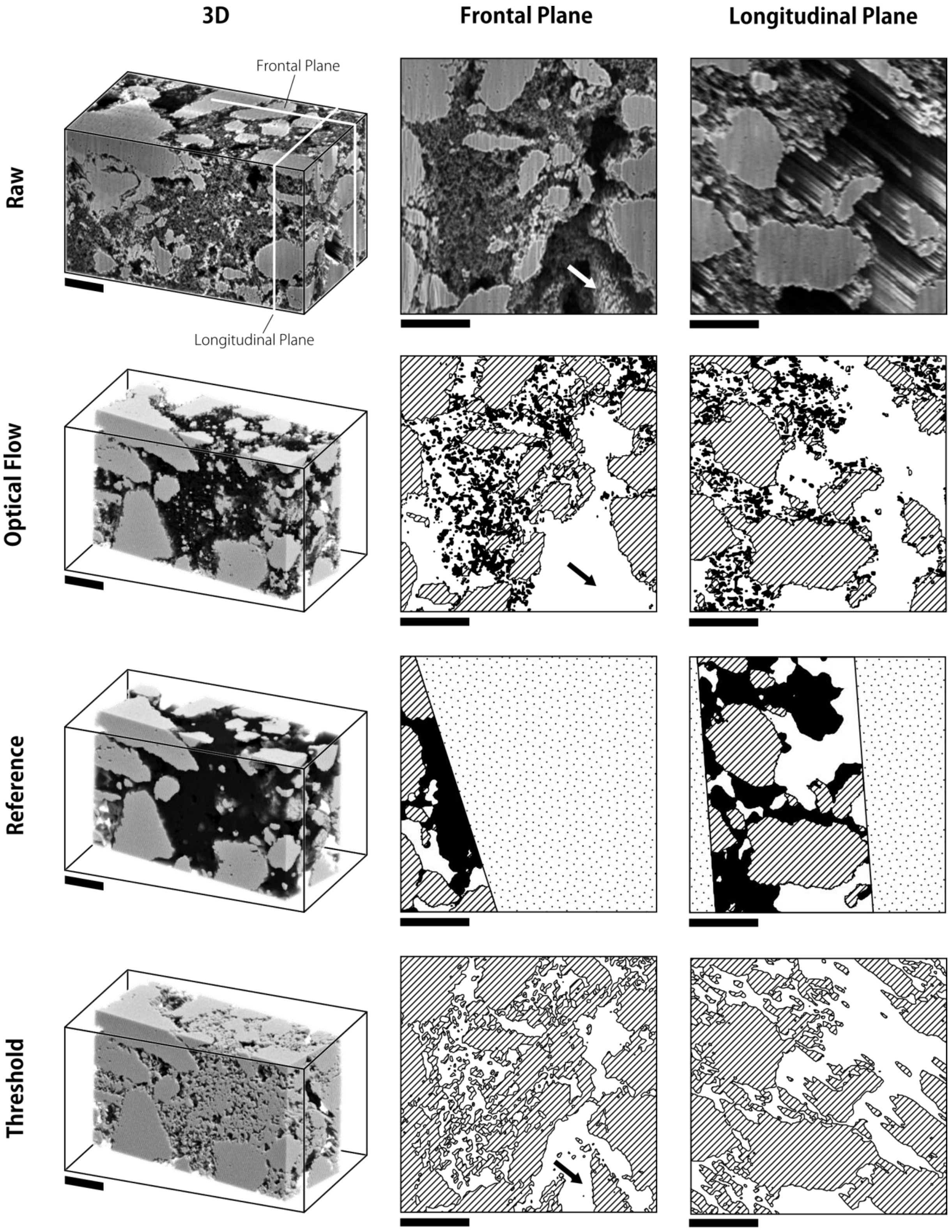

Figure 5: The segmentation results of the LIB composite cathode dataset. The columns show a 3D representation (left) and the central frontal and longitudinal planes (center and right, respectively). The position of the planes is illustrated in the 3D depiction of the raw data (top left). In the second and third row, active material is depicted hatched, while carbon/binder is illustrated as black area. In the dotted regions in the third row no reference segmentation is available. In the fourth row, all solid material is depicted hatched, since the threshold segmentation only distinguishes solid and pore. For comparability, the 3D images of the segmentations are limited to the region where the reference segmentation is available. Each scale bar represents 5 µm.

4. Conclusion

The optical-flow-based segmentation method described in this work allows the partition of FIB/SEM tomography datasets into pore and solid material. The MATLAB implementation that is provided in the supplementary material needs only two unknown parameters: an initial guess for the segmentation, e.g. given by a gray-value threshold value, and the λ' parameter. Due to the short runtime of the program (in the range of minutes on a modern desktop computer for common datasets of about 500 images with 750 × 750 pixels each), proper candidates for both inputs can be guessed by means of trial and error. After fine tuning, the program gives satisfactory to good segmentation results which are significantly better than ordinary gray-value threshold segmentations. Although the program will surely not solve all segmentation issues with FIB/SEM tomographies, it is able to significantly reduce problems with shine-through artifacts and thus can be seen as an image processing filter exactly for this purpose. This is especially valuable since manual segmentation of FIB/SEM tomography datasets is an extremely tedious task, and no such filter is currently available to the broader public.

5. References

[1] D. Banham, S. Ye, Current Status and Future Development of Catalyst Materials and Catalyst Layers for Proton Exchange Membrane Fuel Cells: An Industrial Perspective, ACS Energy Lett. 2 (2017) 629–638. https://doi.org/10.1021/acsenergylett.6b00644.

[2] Y. Tang, Y. Zhang, W. Li, B. Ma, X. Chen, Rational material design for ultrafast rechargeable lithium-ion batteries, Chem. Soc. Rev. 44 (2015) 5926–5940. https://doi.org/10.1039/c4cs00442f.

[3] N. Epstein, On tortuosity and the tortuosity factor in flow and diffusion through porous media, Chemical Engineering Science 44 (1989) 777–779. https://doi.org/10.1016/0009-2509(89)85053-5.

[4] F. Hegge, J. Sharman, R. Moroni, S. Thiele, R. Zengerle, M. Breitwieser, S. Vierrath, Impact of Carbon Support Corrosion on Performance Losses in Polymer Electrolyte Membrane Fuel Cells, J. Electrochem. Soc. 166 (2019) F956-F962. https://doi.org/10.1149/2.0611913jes.

[5] H. Schulenburg, B. Schwanitz, N. Linse, G.G. Scherer, A. Wokaun, J. Krbanjevic, R. Grothausmann, I. Manke, 3D Imaging of Catalyst Support Corrosion in Polymer Electrolyte Fuel Cells, J. Phys. Chem. C 115 (2011) 14236–14243. https://doi.org/10.1021/jp203016u.

[6] S. Thiele, R. Zengerle, C. Ziegler, Nano-morphology of a polymer electrolyte fuel cell catalyst layer—imaging, reconstruction and analysis, Nano Res. 4 (2011) 849–860. https://doi.org/10.1007/s12274-011-0141-x.

[7] L. Holzer, M. Cantoni, Review of FIB tomography, in: I. Utke, S. Moshkalev, P. Russell (Eds.), Nanofabrication using focused ion and electron beams: Principles and applications, Oxford Univ. Press, Oxford, 2012.

[8] M. Salzer, S. Thiele, R. Zengerle, V. Schmidt, On the importance of FIB-SEM specific segmentation algorithms for porous media, Materials Characterization 95 (2014) 36–43. https://doi.org/10.1016/j.matchar.2014.05.014.

[9] L. Holzer, B. Muench, M. Wegmann, P. Gasser, R.J. Flatt, FIB-Nanotomography of Particulate Systems—Part I: Particle Shape and Topology of Interfaces, J American Ceramic Society 89 (2006) 2577–2585. https://doi.org/10.1111/j.1551-2916.2006.00974.x.

[10] M. Ender, J. Joos, T. Carraro, E. Ivers-Tiffée, Quantitative Characterization of LiFePO 4 Cathodes Reconstructed by FIB/SEM Tomography, J. Electrochem. Soc. 159 (2012) A972-A980. https://doi.org/10.1149/2.033207jes.

[11] F. Hegge, R. Moroni, P. Trinke, B. Bensmann, R. Hanke-Rauschenbach, S. Thiele, S. Vierrath, Three-dimensional microstructure analysis of a polymer electrolyte membrane water electrolyzer anode, Journal of Power Sources 393 (2018) 62–66. https://doi.org/10.1016/j.jpowsour.2018.04.089.

[12] S. Vierrath, F. Güder, A. Menzel, M. Hagner, R. Zengerle, M. Zacharias, S. Thiele, Enhancing the quality of the tomography of nanoporous materials for better understanding of polymer electrolyte fuel cell materials, Journal of Power Sources 285 (2015) 413–417. https://doi.org/10.1016/j.jpowsour.2015.03.110.

[13] M. Salzer, A. Spettl, O. Stenzel, J.-H. Smått, M. Lindén, I. Manke, V. Schmidt, A two-stage approach to the segmentation of FIB-SEM images of highly porous materials, Materials Characterization 69 (2012) 115–126. https://doi.org/10.1016/j.matchar.2012.04.003.

[14] T. Prill, K. Schladitz, D. Jeulin, M. Faessel, C. Wieser, Morphological segmentation of FIB-SEM data of highly porous media, J. Microsc. 250 (2013) 77–87. https://doi.org/10.1111/jmi.12021.

[15] M. Salzer, T. Prill, A. Spettl, D. Jeulin, K. Schladitz, V. Schmidt, Quantitative comparison of segmentation algorithms for FIB-SEM images of porous media, J. Microsc. 257 (2015) 23–30. https://doi.org/10.1111/jmi.12182.

[16] MATLAB, The MathWorks, Inc., Natick, Massachusetts, United States, 2018.

[17] T. Brox, A. Bruhn, N. Papenberg, J. Weickert, High Accuracy Optical Flow Estimation Based on a Theory for Warping, in: T. Pajdla, J. Matas (Eds.), Computer Vision - ECCV 2004: 8th European Conference on Computer Vision, Prague, Czech Republic, May 11-14, 2004. Proceedings, Part IV, Springer, Berlin, Heidelberg, 2004, pp. 25–36.

[18] D. Sun, S. Roth, M.J. Black, Secrets of optical flow estimation and their principles, in: IEEE Conference on Computer Vision and Pattern Recognition (CVPR), 2010, San Francisco, CA, USA, IEEE, Piscataway, NJ, 2010, pp. 2432–2439.

[19] M.R. Garey, D.S. Johnson, Computers and intractability: A guide to the theory of NP-completeness, twenty-seventh. print, Freeman, New York u.a, ca. 2009.

[20] K. Katayama, H. Narihisa, Performance of simulated annealing-based heuristic for the unconstrained binary quadratic programming problem, European Journal of Operational Research 134 (2001) 103–119. https://doi.org/10.1016/S0377-2217(00)00242-3.

[21] W.H. Press, Numerical recipes: The art of scientific computing ; source code CD-ROM v 3.0, V third.0, [complete source code in C++], Cambridge Univ. Press, Cambridge, 2007.

[22] S. Thiele, T. Fürstenhaupt, D. Banham, T. Hutzenlaub, V. Birss, C. Ziegler, R. Zengerle, Multiscale tomography of nanoporous carbon-supported noble metal catalyst layers, Journal of Power Sources 228 (2013) 185–192. https://doi.org/10.1016/j.jpowsour.2012.11.106.

[23] R. Moroni, M. Börner, L. Zielke, M. Schroeder, S. Nowak, M. Winter, I. Manke, R. Zengerle, S. Thiele, Multi-Scale Correlative Tomography of a Li-Ion Battery Composite Cathode, Sci. Rep. 6 (2016) 30109. https://doi.org/10.1038/srep30109.

[24] E.H. Adelson, C.H. Anderson, J.R. Bergen, P.J. Burt, J.M. Ogden, Pyramid methods in image processing, RCA engineer 29 (1984) 33–41.